

Reservoir Computing with Random Skyrmion Textures

D. Pinna,^{1,*} G. Bourianoff,^{2,†} and K. Everschor-Sitte¹

¹*Institute of Physics, Johannes Gutenberg-Universität, Mainz 55128, Germany*

²*Intel Corporation, Austin, Texas 78746, USA*



(Received 22 May 2020; accepted 13 October 2020; published 10 November 2020)

The reservoir computing paradigm posits that complex physical systems can be used to simplify pattern recognition tasks and nonlinear signal prediction. We show that random topological magnetic textures pinned by grain inhomogeneities demonstrate desirable dynamical responses for the implementation of reservoir computing as applied to ac current pulses. By harnessing the complex resistance or magnetization responses exhibited by random magnetic skyrmion textures to demonstrate simple pattern recognition, we explain how spintronics systems offer an advantage in the search for an ideal reservoir computer. The dynamical properties of compact skyrmion fabrics, coupled with their CMOS integrability operating on similar length and timescales, open the door for skyrmion-based reservoir computing applications.

DOI: 10.1103/PhysRevApplied.14.054020

I. INTRODUCTION

Reservoir computing [1] (RC) is a computational framework suited for nonlinear, spatial-temporal, history-dependent data processing. It is motivated by how biological systems process and respond to sensory information in the context of the recent past. The general RC classification includes two distinct recursive neural network models, including echo state networks and liquid state machines. Any RC system must include a reservoir for mapping inputs into a high-dimensional space and a one-dimensional readout that can be trained to extract features of the inputs for categorization; see Fig. 1(a). Training is carried out only in the one-dimensional readout layer using linear regression. Thus, the major advantage of RC is fast and simple supervised learning compared to other recurrent neural networks. The reservoir itself undergoes a complex dynamic response to the inputs that, in general evolve on a timescale longer than the characteristic timescale of the inputs. This imparts a fading memory functionality to the system. The reservoir can be directly realized using the internal dynamics of physical systems [2], substrates, and devices, instead of recurrent neural networks; see Fig. 1(b). Here, the dynamic response of the physical system is used to compute, exploiting the fact that matter implicitly stores the correlated physical information defining its dynamical state.

The purpose of this paper is to build on the analyses contained in 20 years of RC literature, as well as two recent works devoted to implementing RC systems with skyrmion fabrics serving as the reservoir [3,4]; see

Figs. 1(c) and 1(d). In this work we relax some of the limitations assumed in the previous works, in particular taking grain inhomogeneities and thermal fluctuations into account (see Sec. II), and extend the analysis to include a more complete (but still limited) analysis of the physical system. In Sec. III we systematically investigate the anisotropic magnetoresistance (AMR) response of the skyrmion fabrics (pinned by grain inhomogeneities) to sinusoidal and square voltage pulse trains as a function of frequency. This enables us to estimate the magnitude of the nonlinear response function of the fabric as distinct from the linear portion. In Sec. IV we numerically demonstrate the proof of concept of RC with skyrmion fabrics. This means that we employ the nonlinear response of the skyrmion fabrics to voltage pulse trains for signal characterization, based on (a) temporal tracing of the reservoir's response and (b) local measurements, exploiting the reservoir's spatial-temporal correlations. We conclude in Sec. V with a discussion of future research requirements, on the road to experimental verification.

II. SKYRMION FABRIC RESERVOIR MODEL

Magnetic skyrmions are compact and metastable magnetic structures predicted over two decades ago [5] and very actively studied experimentally both in lattice [6] and isolated forms [7]. The particlelike properties of skyrmions have been extensively summarized in several reviews [8–13]. Their mobility under ultralow current driving [14, 15] and room-temperature stability [16–21] have garnered them a central position as potential information carriers in many device-relevant materials and applications [22–27]. Device-oriented research has however mostly ignored

*dpinna@protonmail.com

†Retired

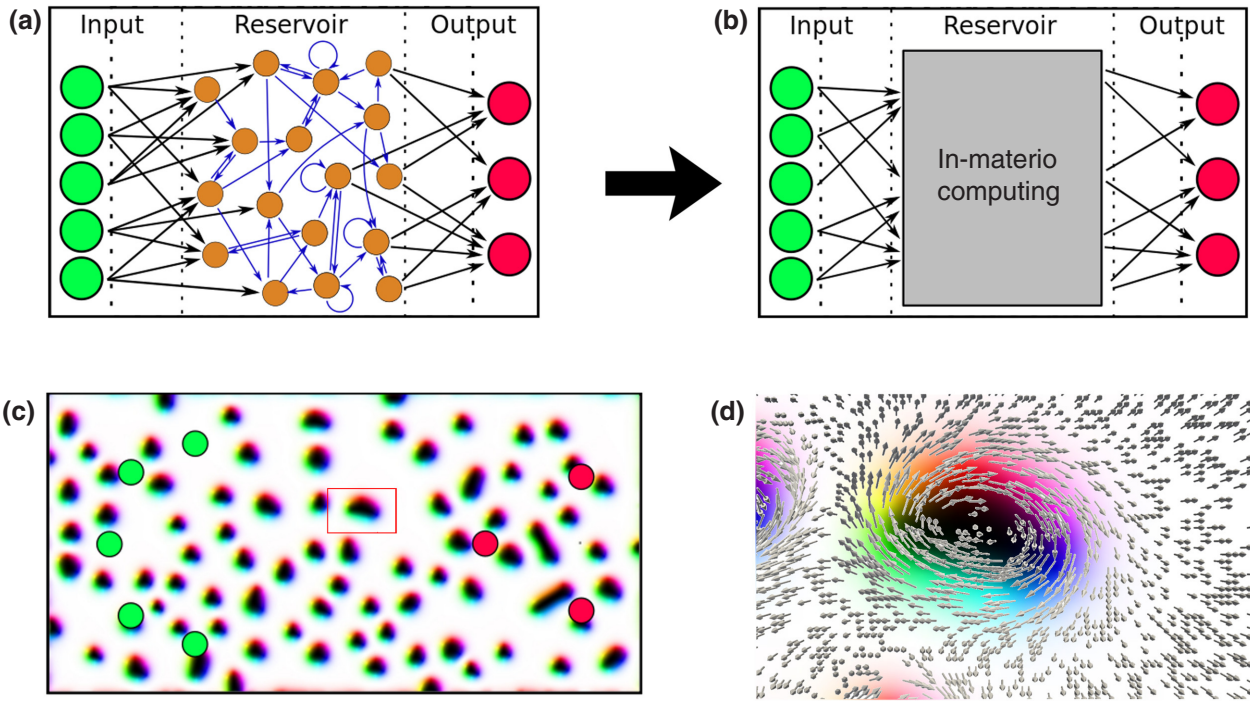


FIG. 1. General setup of reservoir computing for (a) a recurrent neural network and (b) a material-based reservoir. (c) Example of a skyrmion fabric reservoir with the locations of input (output) contacts identified by green (red) circles. The in-plane orientation of the magnetization is color coded and (d) shown in detail with arrows for a sample Bloch skyrmion identified by the red frame in (c).

intermediate skyrmion phases (known as “skyrmion fabrics” [3,4]) that interpolate between single skyrmions, skyrmion crystals, and magnetic domain walls [28].

In this work, we consider a random magnetic skyrmion phase in a spatially extended rectangular geometry with grain inhomogeneities. The skyrmion fabric is excited via time-varying voltage patterns applied between two voltage contacts; see Fig. 2 for an example. Our static model contains the exchange interaction, anisotropy, an applied Zeeman field, magnetostatic interactions as well as the Dzyaloshinskii-Moriya interaction (DMI) with varying strength among the different grains. The magnetic texture we consider is modeled after recently studied Pt/Co/Ir multilayer stacks [29]. The details of the model are summarized in Appendix A. The grain boundaries ensure

the pinning of the skyrmion fabrics [29,30], as a significant displacement of the magnetic texture topology would destroy the echo state property required for classification applications. We test the stability of the chosen skyrmion fabrics with respect to thermal noise; see Appendix A. Furthermore, we perform a stability analysis to determine the maximum excitation voltage that can be applied to the contacts short of inducing skyrmion creep motion across grain boundaries. In this regime, the time-dependent deformations of the magnetic texture due to a variety of magnetoresistive effects [31–33] are maximal.

Since the natural electron relaxation timescale is orders of magnitude smaller than the ferromagnetic resonance (FMR) timescale (approximately 10^{-14} s versus approximately 10^{-9} s), these effects will guarantee that a given

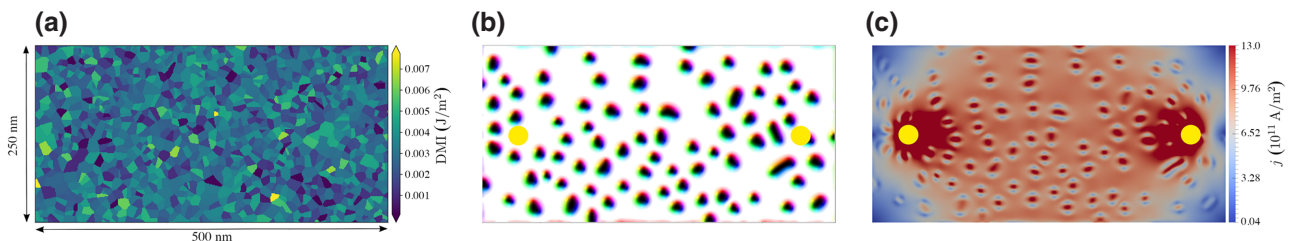


FIG. 2. (a) Randomly generated DMI grain inhomogeneities employed to pin skyrmions. (b) Sample skyrmion texture used for simulations. The locations of the electrical nanocontacts are identified by the yellow circles (size has been enhanced for visibility). (c) Current distribution through the magnetic texture shown in (b) with applied voltage (110 mV) across the nanocontacts.

state of the magnetic texture (stable over the time period of interest) will result in a corresponding unique current distribution throughout the geometry. To simplify the modeling of such electron-transport mediated effects and isolate their qualitative nature, we focus solely on the AMR effect; see Appendix A for details. Additional magnetoelectric interactions between the electrons and magnetic texture will almost certainly exist in physical systems.

III. NONLINEAR ANISOTROPIC MAGNETORESISTIVE RESPONSE

In this section we analyze the magnitude of the AMR response of the skyrmion fabric to voltage pulses applied to the nanocontacts as a function of the driving frequency and reservoir size, and estimate its temperature dependence. We show that the current flow through the magnetic texture extracts and projects essential spatial-temporal features of the applied voltage waveforms in a consistent manner across multiple waveforms and the timescales of interest. This is the basis for spatial-temporal pattern characterization, for which we demonstrate proof of concepts in Sec. IV.

To be more precise, we analyze the texture's AMR response to individual sinusoidal and square pulses of varying frequencies ranging from 0.7 to 5 GHz with 1 ns ‘resting’ intervals between them; see Fig. 3 and Appendix B. The AMR resistance response to individual pulses is found to be quite modest, never exceeding 0.5% at any of the frequencies considered. However, the magnetic texture is seen to remain in a dynamical state past the end of the applied voltage pulses. It requires approximately an extra 0.6 ns for the texture to settle back down to its equilibrium state; see Figs. 3(a) and 3(d).

We next excite the texture with random sequences of square and sinusoidal pulses and observe their resulting AMR responses; see Figs. 3(b) and 3(e) and Appendix B. In order to quantify what fraction of the resistance trace measurement can be considered as the nonlinear response, we construct a hypothetical linear resistance response by linearly superposing the individual pulse responses discussed above.

We observe that at high driving frequencies, see Fig. 3(e), the observed AMR response does not differ significantly from the linearly constructed response. The system is not able to react to the driving signals if the frequencies are too large. This leads to the conclusion that at high frequencies, the system response is essentially linear, i.e., that there is no significant memory functionality at these high frequencies.

For driving frequencies close to the system's natural excitation frequencies, however, the situation is different, and a strong nonlinear resistance response occurs. For the skyrmion fabrics model, the system's natural excitation

frequencies are characterized by the magnetic texture's FMR frequencies, which for our chosen system are of the order of 1 GHz. In this case, the magnetization's out-of-equilibrium dynamics have time to fully interact with the variations in the driving voltage. As the FMR timescale effectively denotes the time taken by the magnetization to respond to its effective field, the magnetization dynamics are maximally responsive to excitation by the applied voltage when the timescales are closely coupled. This is demonstrated in the simulations by the sudden increase in the AMR response amplitude (to values as high as 4%) as the sampled frequencies are lowered to the 0.7–1.8 GHz range; see Appendix B for more frequency data.

When the driving frequency drops below the system's natural timescale, the magnetization relaxes adiabatically to the driving voltage, and thus loses all memory of past pulse information; see Appendix B.

To systematically study how the peak AMR amplitude scales with system size, we generated random textures on $250 \times L \text{ nm}^2$ geometries where the lateral dimension L is allowed to vary between 50 and 500 nm. The voltage applied at the contacts is scaled by the geometry's lateral dimension to compare the current densities across the different simulated samples. Since all other physical parameters are kept identical, altering the sample size only changes the net number of skyrmions participating in the reservoir's response, without altering their density and individual sizes. As expected, the AMR response mostly scales linearly with the lateral size, as shown in Fig. 4(a), or more generally it scales with the area of the skyrmion fabrics reservoir. Thus, the AMR effect's intensity can be increased by increasing the dimensions of the skyrmion fabric.

Aside from the stability tests discussed in Appendix A, all results shown have been obtained via zero temperature micromagnetic simulations. Effects due to thermal noise can, however, significantly affect the magnetic texture's dynamics and, consequently, the measured resistance responses. Currently, full simulations of current transport *and* thermal effects are impractical due to time constraints given our available computational tools. Therefore, to justify a lower bound on the signal-to-noise ratio, we only show the sample's equilibrium AMR as a function of thermal noise; see Fig. 4(b). We find that the equilibrium AMR (in units of the zero temperature magnitude $R_0 \equiv R|_{T=0 \text{ K}}$) scales linearly with temperature up to a room temperature value of approximately 8%. Since the peak AMR measurements of our sample when excited by 1 GHz continuous voltage patterns is registered at approximately 4%, we estimate that AMR signals will still be distinguishable at temperatures up to about 100 K for samples with similar geometries. A more quantitative understanding of these dependencies can only be gleaned from full electron transport simulations through the magnetic texture.

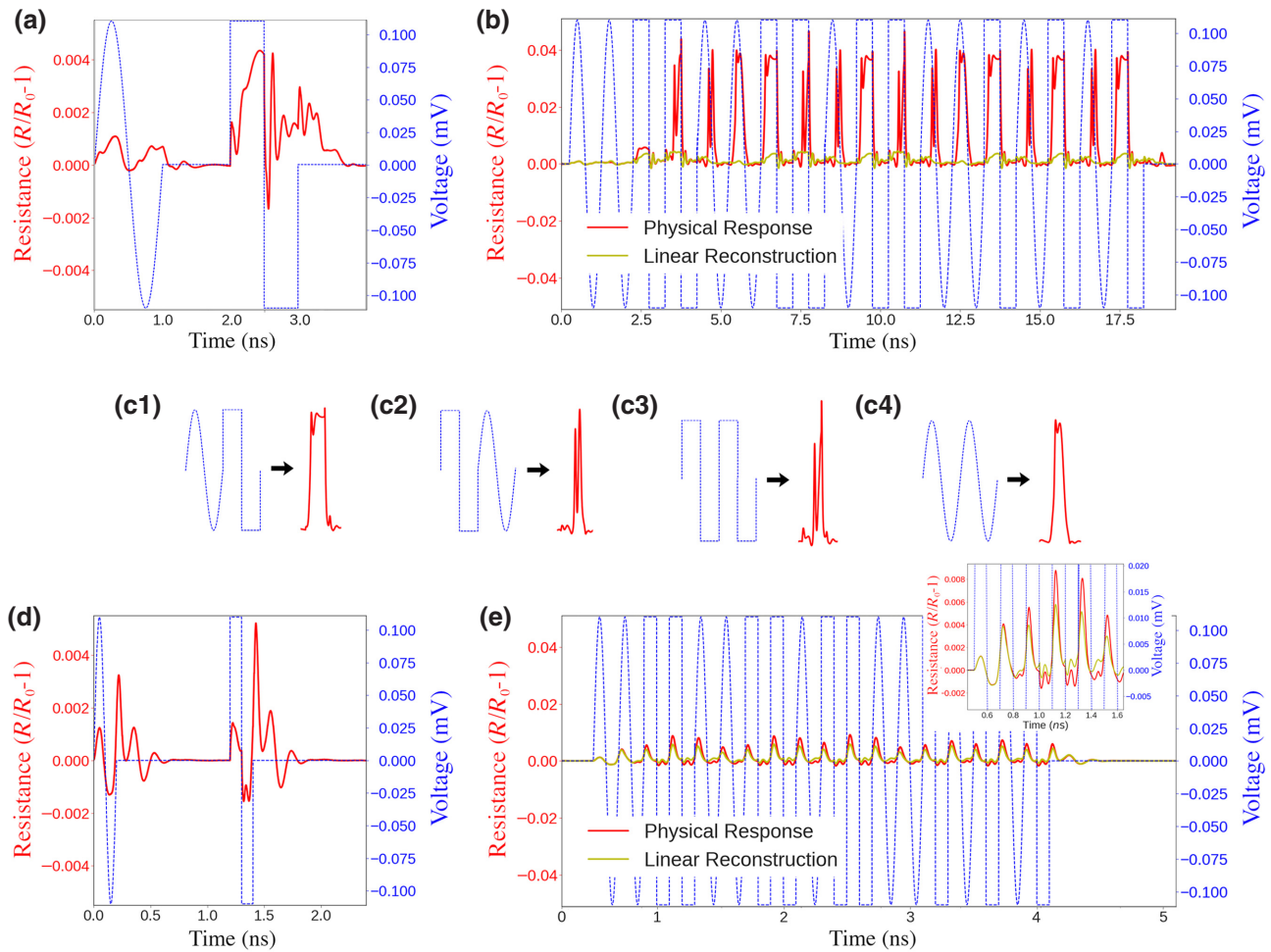


FIG. 3. AMR response (red) of the magnetic texture to individual sine and square voltage pulses (dashed blue) used to drive the magnetization dynamics with frequencies of (a) 1 GHz and (d) 5 GHz. AMR response to identically structured pulse trains used to drive the magnetic texture with varying combinations of sine and square voltage pulses with frequencies of (b) 1 GHz and (e) 5 GHz. Resistances are given in units of R_0 , which denotes the geometry's AMR resistance in the vanishing applied voltage limit. In (a) and (d), the ring down of the magnetic texture is exemplified by the delay between the voltage pulse ending and the AMR relaxation to equilibrium. In (b) and (e), the AMR response observed for individual pulses is superimposed consistently with the driving voltage (yellow) for comparison with the simulated AMR response to emphasize its nonlinear behavior. At frequencies much larger than the system's FMR frequency (e) the magnetic texture's nonlinear evolution does not have sufficient time to respond to the driving voltage patterns, leading to a close match between both the AMR response of (d) the individual pulses as well as (e) the response of the pulse train with its linear reconstruction (see the inset for details). At frequencies comparable with the FMR frequency the magnetization dynamics are highly sensitive to both the instantaneous voltage intensity and memory of past voltage values, presenting a large spike in the peak AMR resistance. This is apparent in both the AMR response to (a) individual sine and square pulses as well as (b) a strong difference between the pulse train's response and the linear reconstruction. We characterize the AMR response observed in (b) by four reproducible and distinct resistance pulse shapes depending on whether a (c1) sine-square, (c2) square-sine, (c3) square-square, or a (c4) sine-sine pulse combination drives the dynamics; for a thorough analysis; see Sec. IV.

IV. PATTERN RECOGNITION

To demonstrate simple temporal pattern recognition, we focus on the 1 GHz AMR response data shown in Fig. 3(b), where the nonlinear signals are largest. In this section, we first present results for temporal and spatial pattern matching utilizing randomly mixed pulse trains of the three pulse sequences, yielding $2^3 = 8$ possible categories. However, before performing a rigorous analysis with three pulse sequences, we note that in the resistance

trace one can visually distinguish at least four reproducible resistance pulse shapes, which are highlighted in Fig. 3(c). We observe that the resistance response to the two pulse sequence is dependent on both of the pulses, not just the most recent pulse. In other words, the skyrmion fabric has a memory. As the voltage pulse train consists of only sine and square waves, we have four possible two-pulse combinations: (c1) sine-square, (c2) square-sine, (c3) square-square, and (c4) sine-sine combinations. This

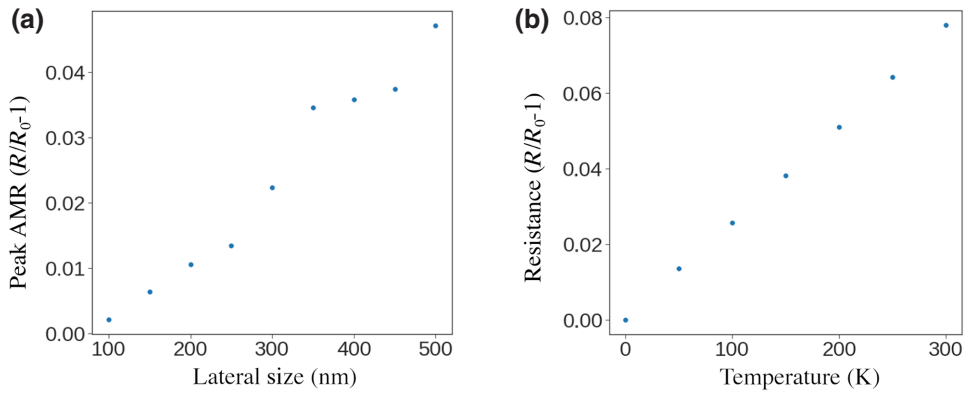


FIG. 4. (a) Example peak AMR response to a 1 GHz pulse train driving as a function of lateral size of the magnetic geometry (vertical size is kept constant). (b) Average equilibrium AMR resistance of a $250 \times 500 \text{ nm}^2$ geometry as a function of temperature in the limit of vanishing applied voltage. As in previous results, resistances are given in units of R_0 , which denotes the zero temperature equilibrium of the $250 \times 500 \text{ nm}^2$ geometry. Combining (a) and (b), we expect that AMR signals will still be qualitatively distinguishable for temperatures below 100 K.

reveals the short-term memory of the skyrmion fabrics for temporally correlated features.

To more precisely quantify these concepts, we train a single feed-forward output layer (standard linear classifier) to attempt recognizing three-pulse sequences of sine and square wave pulses. For this, we simulate the driven dynamics of our skyrmion texture subject to a 400 ns long random pulse train. To exemplify the reservoir computing properties, the training set consists of only one example of each three-pulse sequence and sampling of our reservoir state is performed in two different ways to compare memory performance—time tracing the reservoir’s resistance response and spatially sampling the magnetic texture. For both techniques, we refer to the *present pulse* as the present pulse driving the system, the *latent pulse* as that which preceded the present pulse, and the *past pulse* as that preceding the latent pulse; see Fig. 5. In the following, we present the results of both techniques and then discuss them. For more details on the reservoir training, we refer the reader to Appendix C.

A. Reservoir computing based on tracing the reservoir’s response in time

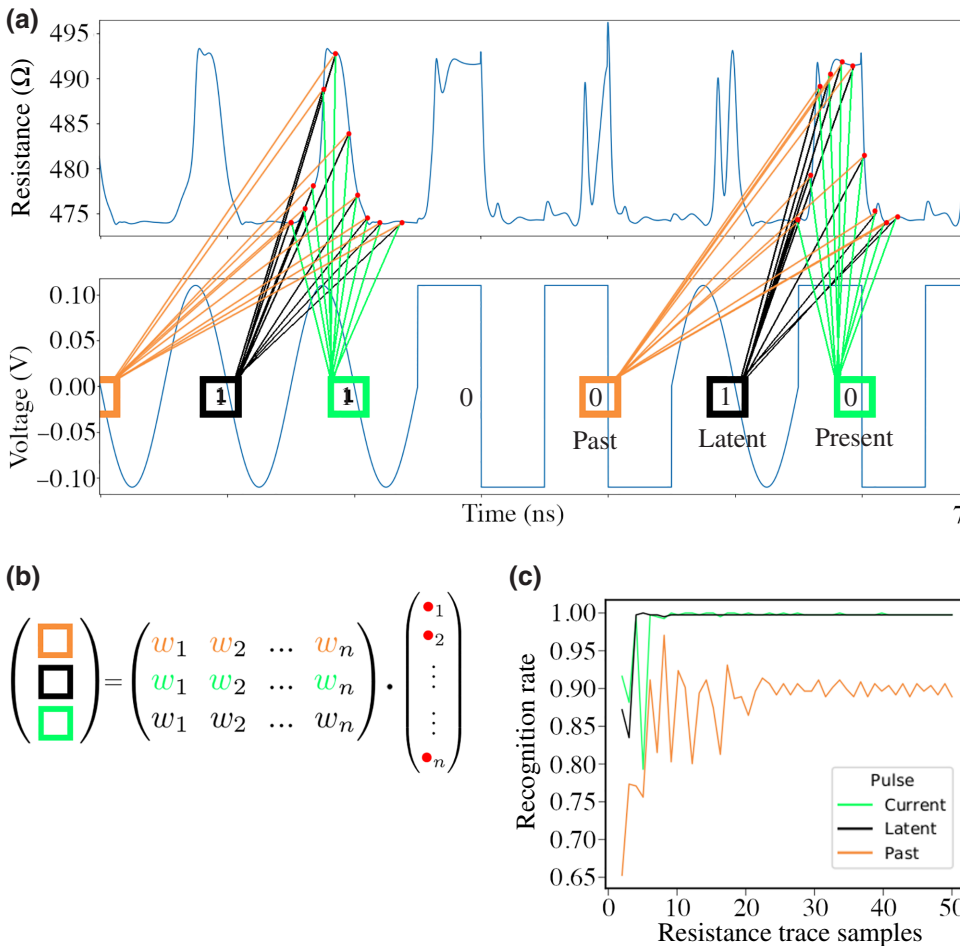
For the first technique, we sample the time-resolved AMR response at regular intervals across the time window corresponding to the present pulse driving; see Fig. 5(a). This results in a vector of resistance values of dimension fixed by the number of samples chosen. As schematically shown in Fig. 5(b), and explained further in Appendix C, these resistance values are summed in weight to generate a recognition of present, latent, and past pulses. In Fig. 5(c) we display the recognition rates of the present, latent, and past pulses as a function of the number of resistance samples, demonstrating the success of this method. These high

recognition rates (greater than 98% for the current and latent pulses and greater than 85% for the past pulse) are valid down to approximately ten resistance samples, showing how this technique could potentially be viable as long as the resistance can be time resolved down to about the 0.1 ns timescale. Note that 50% would be associated with pure random probability.

B. Reservoir computing based on resolving the reservoir’s response in space

To avoid time resolution constraints, a second technique is also possible where the spatial information of the sample is used. We suggest sampling the magnetic state spatially directly on the magnetic texture. This is in principle possible if the local magnetic field components in the magnetic texture can be locally measured and extracted through, for example, an array of nanocontacts. While this is a daunting task that is beyond the reach of current technology, we emphasize that any other nonlinear spatial readout would also work, such as measuring local resistances. In our model, we implement the local magnetization readout functionality, by creating a regular 5×6 grid of 20 nm^2 regions separated 20 nm from their neighbors, as schematically shown in Fig. 6(a). In each region we calculate the average out-of-plane component of the magnetization at a specific instant during the present pulse. As for the time-multiplexing case, this array of average magnetization values is trained via a linear classifier on our minimal eight-pulse training set and used to recognize the present, latent, and past pulses of our 400 ns dataset.

In Figs. 6(b)–6(d) we show the pattern recognition results as a function of the number of readout elements used, color coded according to the time offset of their snapshot as measured from the beginning of the present pulse.



From Fig. 6(b) we see that taking a snapshot at the beginning of the present pulse results in a 50% recognition rate of the present pulse itself, as expected. This is due to the fact that at this time the reservoir has no information about

the present pulse. Once some information about the present pulse is revealed, the recognition rate quickly raises. In Fig. 6(c), we see that the recognition rates for the latent pulse are higher for smaller offsets. This is consistent with

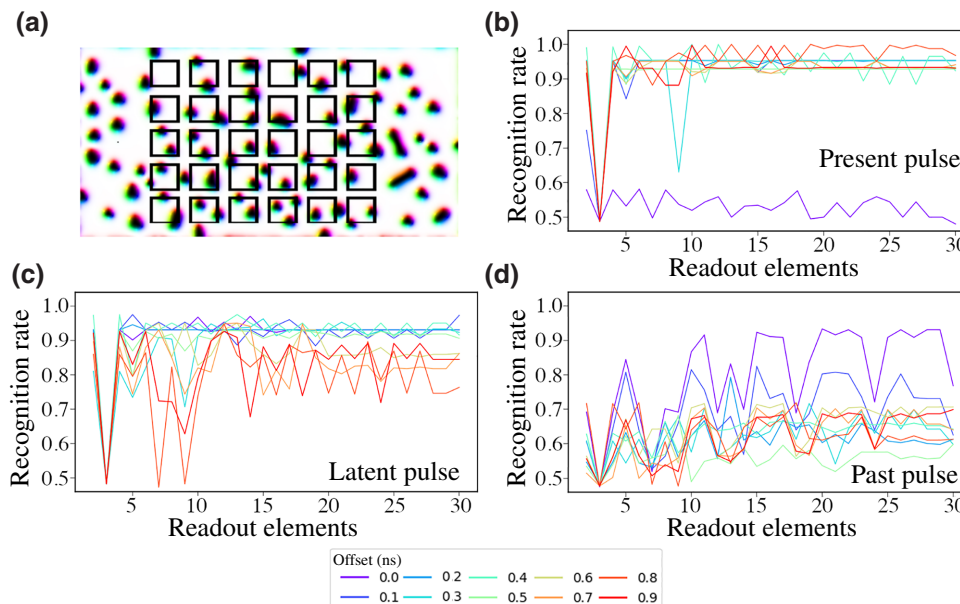


FIG. 5. (a) Schematic of the time tracing used to train and operate the output layer (temporal axis is common for both voltage and resistance plots). The resistance response is sampled at regular intervals across the temporal window of the instantaneous—present—pulse driving the magnetic texture. (b) These resistance values are summed in weight for three different sets of weights. One set is trained to recognize the present pulse currently driving the system, the second set is trained to recognize the latent pulse preceding the present pulse, and the third set is trained to recognize the past pulse preceding the latent pulse. (c) Recognition rates of the pulses as a function of the number of resistance trace samples chosen.

FIG. 6. (a) Schematic of the readout element grid used to measure averages of the out-of-plane component of the magnetic texture. Recognition rates of the voltage pulses (b) present, (c) latent, and (d) past to the readout measurement as a function of the number of grid elements used. Color coding corresponds to offset time from the beginning of the present pulse. At a 0 ns offset, the recognition rate of the present pulse is 50% as no information about the voltage pulse is actually present in the magnetic texture.

the idea that information is lost over time due to dissipative effects. Finally, in Fig. 6(d) we see how the recognition rate for the past pulse drops dramatically as a function of increasing offset. The probabilities still remain appreciably above 50%, denoting some correlation between the transient magnetic state as opposed to the no-offset recognition rates of the present pulse at a 0 ns offset.

C. Comparison and discussion of pattern recognition results

The two approaches presented—temporal tracing and spatially sampling—are not mutually exclusive, and can in fact be used in tandem to increase the dimensionality of the output sampling space and optimize the pattern recognition performance. While many of the examples presented in the literature [34–38] do not allow for such an arbitrary tunability of the dimensionality of input and output layers, the skyrmion fabrics naturally provide this functionality. This allows for a true RC implementation where unstructured data may be injected without any preprocessing and the reservoir state sampled via instantaneous, real-time, snapshots. Furthermore, the spatially extended nature of such a magnetic system allows for an additional tunability in the number of electrical contacts, which then also contributes to the dimensionality of the reservoir snapshot.

In both RC approaches presented, we emphasize that the training is performed on a very limited set of data consisting of only one example per three-pulse sequence, due to our computationally limited resources. The minimum training set size can be expected to grow as a function of the complexity of pattern recognition required and potential noise in the system. For example, the minimal contribution of the past pulse to the current magnetic state, which allows the time multiplexing to capture and be used for recognition, is likely to be washed out by any randomizing effects, such as thermal effects.

V. DISCUSSION AND CONCLUSION

In this work we have demonstrated that magnetic skyrmion fabrics can, in principle, be employed for RC applications. The recursive dynamic response of the underlying magnetization dynamics excited by the applied signal provides intrinsic memory functionality useful for identifying and characterizing feature correlations of input driving voltages. The gigahertz speeds exhibited by such textures offer potentially faster classification operations compared to the inference times of cutting edge digital neural network techniques (greater than or equal to 10 ms). By contrast, a magnetic reservoir such as the one described, in principle, could reduce inference times by several orders of magnitude. This is especially so if the RC device is designed

to not require complex preprocessing of inputs as regularly done in many RC schemes. A natural extension for even faster processing could eventually be offered by antiferromagnetic materials where the magnetization dynamics evolve up to terahertz speeds.

Major concerns would center around generally low signal levels associated with magnetoresistive effects and the role of thermal scattering that would tend to mask the magnetoresistive effects. Experimental realization of the physical system described here will require improvements in injecting and extracting currents into the skyrmion fabric through nanometer scale contact pads.

In this work we have only considered the AMR contribution to the physics as a magnetoresistive effect but, realistically, many more effects may play a role [31–33]. Among these, the noncollinear magnetoresistance has even been suggested as a reliable all-electrical detection scheme for magnetic skyrmions [32]. Moreover, a better analysis of thermal effects needs to be developed. Thermal effects are not necessarily detrimental to RC-based approaches and will serve to help achieve the fading memory requirement necessary to achieving the echo state property.

To put our work into a broader context, the most intriguing and unique aspect of using skyrmion fabric-based RC from the standpoint of reproducing biological information processing capabilities lies in the inherent capability to seamlessly enable sensor fusion. Biological systems simultaneously process information streaming in from all five senses simultaneously. Another intriguing aspect of magnetic systems for neuromorphic computing are the multiple timescales for the magnetic response, some of which are directly compatible with modern electrons (few gigahertz) in addition to longer timescales associated with plasticity and adaptivity.

A primary barrier to industrial application of utilizing magnetic systems for RC computing is the generally low signal levels (which are generally less than 1%). While such low signal levels are measurable in the laboratory, they are not practical for commercial applications. Fortunately, there are numerous pathways to improving the magnitude of the response but some of which may require full electromagnetic simulation codes in realistic material systems to analyze. On the plus side, the spatial complexity of skyrmion fabrics create high-dimensional phase spaces for information projection and subsequent characterization similar to what is thought to happen in biological systems. Also on the plus side, industry has greatly improved its capability to process, measure, and manufacture magnetic materials and devices due to the advent of magnetic memories.

To summarize, our results represent a basic proof of concept for the foundational role that nanometer-sized spintronics devices [39,40] can play in the development of such technologies.

ACKNOWLEDGMENTS

This work is funded by the German Research Foundation (DFG) under Grants No. EV 196/2-1 and No. TRR 173 – 268565370. We acknowledge funding from the Emergent AI Center funded by the Carl-Zeiss-Stiftung. We thank K. Litzius, J.-V. Kim, S. Kreiss, and J. Sun for fruitful discussions.

APPENDIX A: METHODS

1. Micromagnetic model

The magnetization dynamics are obtained numerically by solving the Landau-Lifshitz-Gilbert (LLG) equation for the unit rescaled magnetization $\mathbf{m} = \mathbf{M}/M_s$ with spin-transfer-torque effects [41,42]:

$$\begin{aligned} (\partial_t + \xi \mathbf{j}[U, \mathbf{m}] \cdot \nabla) \mathbf{m} &= -\gamma \mathbf{m} \times (\mathbf{B}_{\text{eff}} + \mathbf{B}_{\text{th}}) \\ &\quad + \alpha \mathbf{m} \times \left(\partial_t + \frac{\beta}{\alpha} \xi \mathbf{j}[U, \mathbf{m}] \cdot \nabla \right) \mathbf{m}. \end{aligned} \quad (\text{A1})$$

Here $\xi = P\mu_B/(eM_S)$, and M_S , P , μ_B , e are the saturation magnetization, current polarization, Bohr magneton, and electron charge, respectively. Ambient temperature effects can be included through the thermal field term B_{th} :

$$\langle \mathbf{B}_{\text{th}} \rangle = 0, \quad (\text{A2})$$

$$\langle B_{\text{th},i}(t) B_{\text{th},j}(t') \rangle = 2\alpha D \frac{k_B T}{\gamma M_S} \delta_{i,j} \delta(t - t'). \quad (\text{A3})$$

Here $k_B T$ is the thermal energy and $\langle \cdot \rangle$ represents averaging over noise realizations. The effective field \mathbf{B}_{eff} in Eq. (A1) is given by $\mathbf{B}_{\text{eff}} = -M_S^{-1}(\delta F[\mathbf{m}]/\delta \mathbf{m})$, where the micromagnetic free energy comprising exchange, anisotropy, and dipolar interactions is

$$\begin{aligned} F &= \int \left(A_{\text{ex}}(\nabla \mathbf{m})^2 + K_u(1 - m_z^2) - \frac{\mu_0}{2} M_S \mathbf{m} \cdot \mathbf{H}_d(\mathbf{m}) \right) dV \\ &\quad + \int D_B \mathbf{m} \cdot (\nabla \times \mathbf{m}) dV, \end{aligned} \quad (\text{A4})$$

where the last term describes the Bloch DMI [43–45].

The current densities $\mathbf{j}[U, \mathbf{m}]$ are calculated self-consistently through $\mathbf{j}[U, \mathbf{m}] = -\sigma[\mathbf{m}] \cdot \mathbf{E}[U]$ at each time step of the magnetization's LLG dynamics [46], as in Refs. [3,4]. The electric field through the texture, induced by the applied voltage, is calculated by solving the Poisson equation $\mathbf{E} = -\nabla \Phi$ with boundary conditions $\Phi|_{c1} = -\Phi|_{c2} = U$ at the two contacts, and the conductivity tensor $\sigma[\mathbf{m}] = (1/\rho_{\perp})\mathbb{1} + (1/\rho_{\parallel} - 1/\rho_{\perp})\mathbf{m} \otimes \mathbf{m}$ is computed at each point throughout the geometry. We denote by ρ_{\perp} (ρ_{\parallel}) the current resistivities for flows perpendicular (parallel) to the magnetization direction. For definiteness, we consider the typical case where $\rho_{\perp} > \rho_{\parallel}$.

2. Simulation details

The micromagnetic simulations are performed using the MuMax3 GPU-accelerated micromagnetic simulation program [47] for fast magnetization relaxation and the Micromagnum simulation program [48] with custom AMR module [46]. In all simulations, the thickness of the magnetic geometry is 1 nm. The magnetic parameters used in the simulations are as follows: saturation magnetization $M_S = 956$ kA/m, exchange stiffness $A_{\text{ex}} = 10$ pJ/m, Bloch DMI constant $D = 3$ mJ/m², perpendicular magnetic anisotropy constant $K_u = 0.717$ MJ/m³, and applied magnetic field $B_{\text{ext}} = 400$ mT. The Gilbert damping coefficient α is set to 0.2 and the current polarization to 0.5. To pin the skyrmions and preclude them from displacing, we introduce magnetic inhomogeneities by tessellating the entire geometry with Gaussian-distributed grains with an average size of 10 nm and allow for fluctuations in the DMI constant with a 40% variance. Note that, for ultra-thin layers of a couple atoms, local thickness variations of as little as one atom can dramatically change thickness-dependent anisotropies, DMI, etc., by up to 75% [49]. All models are discretized into cubic cells with a constant cell size of $1 \times 1 \times 1$ nm³ in the simulations. The linear size of the cells is smaller than both the fundamental length scale $A_{\text{ex}}/D \simeq 3.3$ nm and the domain wall width $\sqrt{A_{\text{ex}}/K_u} \simeq 3.7$ nm. With these parameters, we observe the stabilization of skyrmions with an average diameter of approximately 30 nm across temperatures ranging from zero to room temperature.

We generally consider a rectangular geometry of planar dimensions $250 \times L$ nm², where L is allowed to vary from 100 to 500 nm (main results in the paper are shown for the case $L = 500$ nm). Electrical nanocontacts are modeled as gold cylinders with a diameter of 1 nm symmetrically located along the x axis of the geometry at positions 0.1 L and 0.9 L . To self-consistently compute the AMR-mediated current density distribution through the magnetic texture, we choose to model a system where we define the conductivity $\sigma_0 = (1/\rho_{\parallel} + 2/\rho_{\perp})/3$ and the ratio of nonadiabatic to adiabatic spin-transfer torque $\beta/\alpha = 0.02$, and consider an AMR ratio [3,46] of $a = 2(\rho_{\parallel} - \rho_{\perp})/(\rho_{\parallel} + \rho_{\perp}) = 1.0$. The voltage patterns injected through the contacts to excite the texture are varied in frequency from 0.7 to 5 GHz, while the voltage amplitude is set to $V = 110(L/L_0)$ mV (where $L_0 = 500$ nm), such that simulation results of geometries with different lateral dimensions could be compared.

3. Initialization of the magnetic texture and stability test

We generate the random magnetic textures used for our simulations via the following protocol, which is depicted in Fig. 7. First, we impose an initial skyrmion lattice structure [Fig. 7(a)] and then allow it to freely relax [Fig. 7(b)].

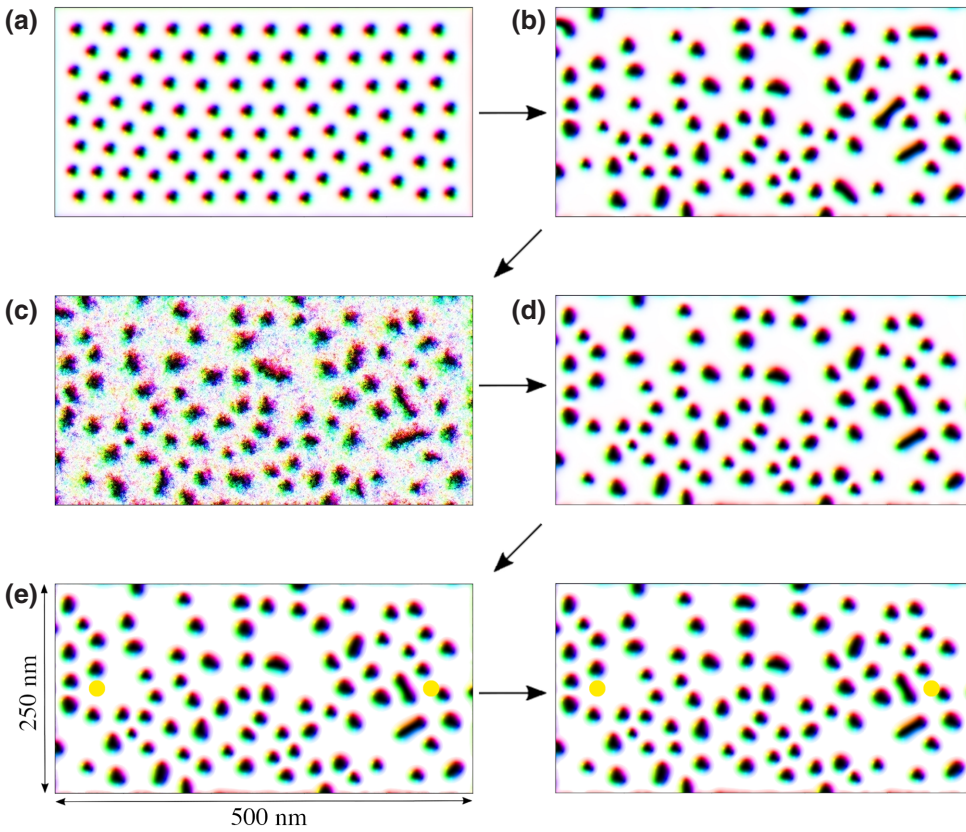


FIG. 7. Initialization of the magnetic texture and thermal stability test. (a) An artificial skyrmion lattice is generated. (b) The lattice is relaxed under the effect of an applied external magnetic field and DMI grain inhomogeneities. (c) Thermal noise is added and allowed to act for 20 ns before being switched off. (d) The magnetic texture is relaxed again in the absence of thermal noise. (e) A 20 ns constant voltage pulse is applied to verify that skyrmions are not displaced by current-mediated transport effects.

Starting from this state we perform stability tests. On the one hand, we apply thermal noise [Fig. 7(c)] and subsequently relax the magnetic structure again in the absence of thermal noise. The relaxed magnetic configurations in (b) and (d) are compared to verify that the majority of skyrmions appearing in the bulk of the geometry are not significantly affected by thermal effects. On the other hand, we apply voltages [Fig. 7(e)] and then relax the structures again, to verify that acting spin torques are small enough that the skyrmions are not displaced significantly. The voltage magnitude is chosen such that the resulting magnetization dynamics lie just below the skyrmion creep threshold where their deformations are maximal.

We consider initialization complete when the magnetic texture has relaxed to a stable state and does not change significantly when subject to thermal noise and a constant applied voltage across the electrical contacts.

APPENDIX B: MEMORY AND AMR RESPONSE BEHAVIOR AT VARYING FREQUENCIES

Here, we provide further AMR response results with the aim to show how they behave as the driving signal frequency is varied around the system's natural dynamical timescale. In Fig. 8 we plot single and pulse train results, analogous to those discussed in Fig. 3, for frequencies below the system's natural frequency, i.e., panels (a) and (b), and for those above 1 GHz, i.e., panels (c) to (f). At

a driving frequency of 0.7 GHz, the driving signal does not change quickly enough to keep the magnetic texture in a transient dynamical state. As such, the texture relaxes adiabatically, not retaining much memory of the driving signal's pulse sequence. Brief AMR spikes are seen in accordance with the square pulses. We believe that these might be exaggerated due to the instantaneous rise time used in the simulations.

Driving frequencies of 1.6 and 1.8 GHz enter a regime that tests the magnetic texture's ability to properly track the driving voltage signal. The pulse train AMR simulations show behavior consistent with the 1 GHz simulations discussed in the text. The peak AMR resistance does not change significantly with these slightly larger frequencies, further suggesting that the total AMR percentage is set by the sample geometry's dimensions. Note that, due to the higher frequency, the reservoir's response can, in principle, allow us to characterize more pulses in the past. At even larger frequencies, as discussed in the main text, the texture decouples from the long-temporal details of the driving signal as it begins to respond linearly to the instantaneous pulse driving.

APPENDIX C: RESERVOIR TRAINING

We use two different techniques to perform reservoir computing. One is based on time tracing the reservoir's resistance response and the other on spatially sampling

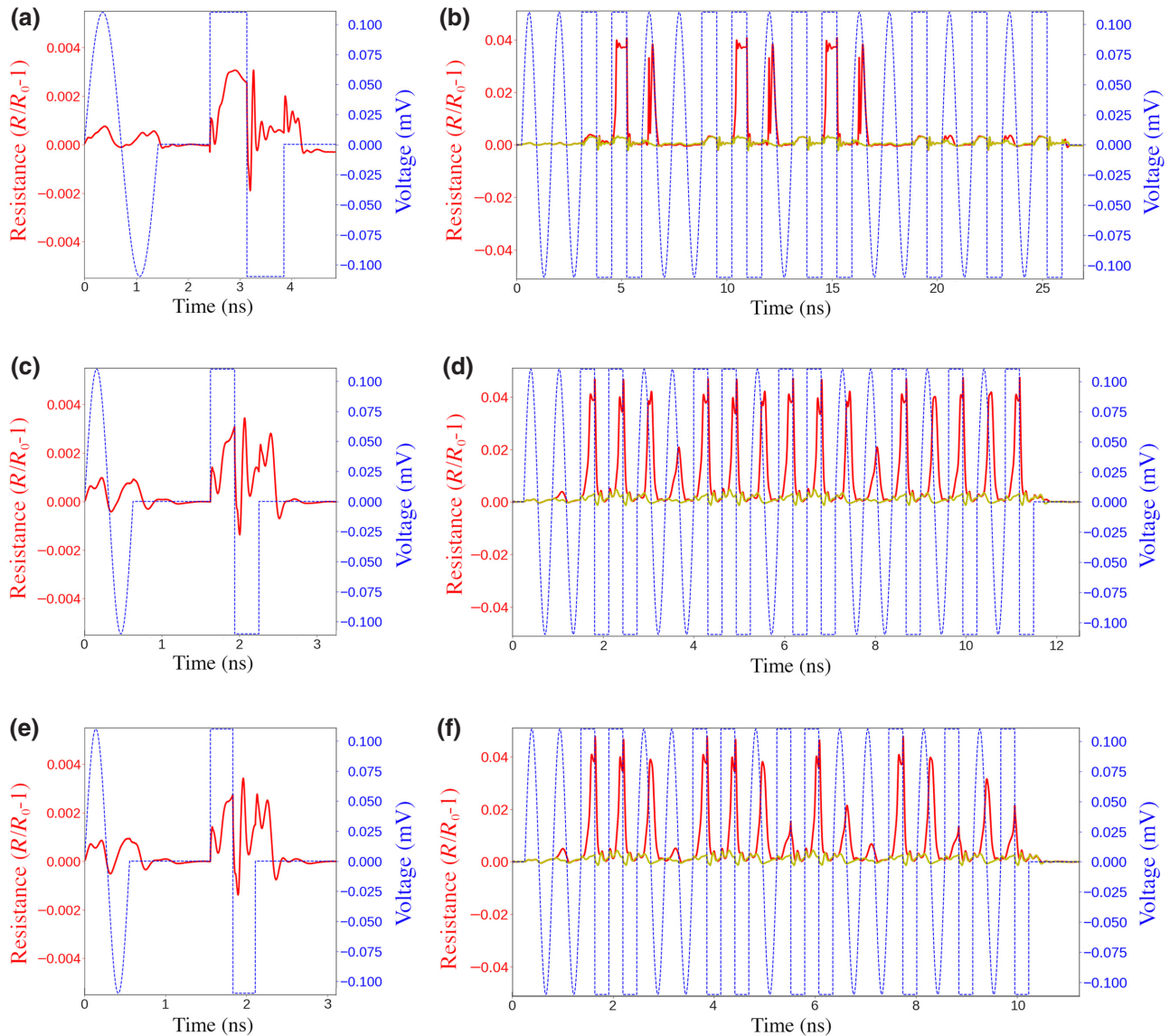


FIG. 8. Single and pulse train AMR response simulations for varying frequencies as discussed in Sec. IV: (a),(b) 0.7 GHz; (c),(d) 1.6 GHz; (e),(f) 1.8 GHz.

the magnetic texture. To describe both of them simultaneously, we first present the general formalism and then put the general notation into context for each of the two techniques.

Denote by $\mathbf{m}(t)$ the state of the reservoir at time t . Training the output layer of a reservoir requires finding the optimal $D \times N$ weight matrix $\hat{\mathbf{W}}$ mapping some sampling $\mathbf{x} \in \mathbb{R}^D$ of \mathbf{m} into a set of N output nodes \mathbf{y} , such that the computed output $\mathbf{y} = \hat{\mathbf{W}} \cdot \mathbf{x}$ minimizes the error $E(\mathbf{y}, \mathbf{y}_T)$ with respect to some target output $\mathbf{y}_T(t)$, i.e.,

$$E(\mathbf{y}(t), \mathbf{y}_T(t)) = \sqrt{\langle \|\mathbf{y}(t) - \mathbf{y}_T(t)\|^2 \rangle}, \quad (C1)$$

where $\|\cdot\|$ stands for the Euclidean norm and $\langle \cdot \rangle$ is an average over all training data. Each element $y_i = \hat{W}_{i,j} x_j$ of the output vector corresponds to the value of a given output node. The categorization of the output state is typically defined by the sign of each of the outputs y_i . Thus, N output nodes allow us to codify 2^N distinct categories. Once the weights in $\hat{\mathbf{W}}$ have been set, the equation $\hat{W}_{i,j} x_j = 0$ effectively describes a D -dimensional hyperplane in the state space of the reservoir. Since N of them need to be specified, *training* means tessellating the reservoir state space with N D -dimensional hyperplanes, whereas *inference* is the task of identifying in which tessellation the reservoir state \mathbf{m} is in.

To parallel between this notation and the skyrmion reservoir system presented in this work, we note the following.

(a) The state $\mathbf{m}(t)$ is the evolution of the infinite-dimensional magnetic texture over time.

(b) The input vector is \mathbf{x} . For time multiplexing, it consists of the resistance time traces sampled at precise temporal intervals $\tau: R[\mathbf{m}](t + n\tau)$. For space multiplexing, it corresponds to the coarse-grained snapshots of \mathbf{m} .

(c) Here $\mathbf{y}(t)$ is the set of nodes necessary to identify all the categories needed for input data classification is. For n -pulse sequences of sine and square wave pulses, there are 2^n possible distinct output categories. Therefore, \mathbf{y} needs to be an n -dimensional vector.

For both the time- and space-multiplexed pattern recognitions, the sampled state data are run through a support vector machine classifier with linear kernel for training and testing. The time-multiplexed data consists of regularly spaced samples of the time-resolved resistance data. For the space-multiplexed data, a 5×6 grid of 20 nm^2 regions with 20 nm interneighbor spacing is used as a mask to calculate the average out-of-plane magnetization components. As only eight possible three-pulse combinations exist, our training set consists of eight different three-pulse sequences. When varying the number N of readout elements in the space-multiplex technique, the N specific elements used are chosen such as to give a homogeneous sampling of the readout grid.

-
- [1] H. Jaeger, M. Lukoševičius, D. Popovici, and U. Siewert, Optimization and applications of echo state networks with leaky-integrator neurons, *Neural Netw.* **20**, 335 (2007).
 - [2] G. Tanaka, T. Yamane, J. B. Héroux, R. Nakane, N. Kanazawa, S. Takeda, H. Numata, D. Nakano, and A. Hirose, Recent advances in physical reservoir computing: A review, *Neural Netw.* **115**, 100 (2019).
 - [3] D. Prychynenko, M. Sitte, K. Litzius, B. Krüger, G. Bourianoff, M. Kläui, J. Sinova, and K. Everschor-Sitte, Magnetic Skyrmion as a Nonlinear Resistive Element: A Potential Building Block for Reservoir Computing, *Phys. Rev. Appl.* **9**, 014034 (2018).
 - [4] G. Bourianoff, D. Pinna, M. Sitte, and K. Everschor-Sitte, Potential implementation of reservoir computing models based on magnetic skyrmions, *AIP Adv.* **8**, 055602 (2018).
 - [5] A. N. Bogdanov and D. A. Yablonskii, Thermodynamically stable “vortices” in magnetically ordered crystals. The mixed state of magnets., *Sov. Phys. JETP* **68**, 101 (1989).
 - [6] S. Mühlbauer, B. Binz, F. Jonietz, C. Pfleiderer, A. Rosch, A. Neubauer, R. Georgii, and P. Böni, Skyrmion lattice in a chiral magnet, *Science* **323**, 915 (2009).
 - [7] N. Romming, C. Hanneken, M. Menzel, J. E. Bickel, B. Wolter, K. von Bergmann, A. Kubetzka, and R. Wiesendanger, Writing and deleting single magnetic skyrmions, *Science* **341**, 636 (2013).
 - [8] N. Nagaosa and Y. Tokura, Topological properties and dynamics of magnetic skyrmions, *Nat. Nano* **8**, 899 (2013).
 - [9] G. Finocchio, F. Büttner, R. Tomasello, M. Carpentieri, and M. Kläui, Magnetic skyrmions: From fundamental to applications, *J. Phys. D: Appl. Phys.* **49**, 423001 (2016).
 - [10] A. Fert, N. Reyren, and V. Cros, Magnetic skyrmions: Advances in physics and potential applications, *Nat. Rev. Mater.* **2**, 1 (2017).
 - [11] W. Jiang, G. Chen, K. Liu, J. Zang, S. G. te Velthuis, and A. Hoffmann, Skyrmions in magnetic multilayers, *Phys. Rep.* **704**, 1 (2017).
 - [12] K. Everschor-Sitte, J. Masell, R. M. Reeve, and M. Kläui, Perspective: Magnetic skyrmions—overview of recent progress in an active research field, *J. Appl. Phys.* **124**, 240901 (2018).
 - [13] C. H. Back, V. Cros, H. Ebert, K. Everschor-Sitte, A. Fert, M. Garst, T. Ma, S. Mankovsky, T. Monchesky, and M. V. Mostovoy *et al.*, The 2020 skyrmionics roadmap, *J. Phys. D: Appl. Phys.* **53** (2020).
 - [14] F. Jonietz, S. Mühlbauer, C. Pfleiderer, A. Neubauer, W. Münzer, A. Bauer, T. Adams, R. Georgii, P. Böni, R. A. Duine, K. Everschor, M. Garst, and A. Rosch, Spin transfer torques in MnSi at ultralow current densities., *Science* **330**, 1648 (2010).
 - [15] T. Schulz, R. Ritz, A. Bauer, M. Halder, M. Wagner, C. Franz, C. Pfleiderer, K. Everschor, M. Garst, and A. Rosch, Emergent electrodynamics of skyrmions in a chiral magnet, *Nat. Phys.* **8**, 301 (2012).
 - [16] X. Z. Yu, Y. Onose, N. Kanazawa, J. H. Park, J. H. Han, Y. Matsui, N. Nagaosa, and Y. Tokura, Near room-temperature formation of a skyrmion crystal in thin-films of the helimagnet FeGe, *Nat. Mat.* **10**, 106 (2011).
 - [17] X. Z. Yu, N. Kanazawa, W. Z. Zhang, T. Nagai, T. Hara, K. Kimoto, Y. Matsui, Y. Onose, and Y. Tokura, Skyrmion flow near room temperature in an ultralow current density., *Nat. Commun.* **3**, 988 (2012).
 - [18] D. A. Gilbert, B. B. Maranville, A. L. Balk, B. J. Kirby, P. Fischer, D. T. Pierce, J. Unguris, J. A. Borchers, and K. Liu, Realization of ground-state artificial skyrmion lattices at room temperature, *Nat. Commun.* **6**, 8462 (2015).
 - [19] O. Boulle, J. Vogel, H. Yang, S. Pizzini, D. de Souza Chaves, A. Locatelli, T. O. Menteş, A. Sala, L. D. Budă-Prejbeanu, and O. Klein *et al.*, Room-temperature chiral magnetic skyrmions in ultrathin magnetic nanostructures, *Nat. Nanotechnol.* **11**, 449 (2016).
 - [20] S. Woo, K. Litzius, B. Krüger, M.-Y. Im, L. Caretta, K. Richter, M. Mann, A. Krone, R. M. Reeve, and M. Weigand *et al.*, Observation of room-temperature magnetic skyrmions and their current-driven dynamics in ultra-thin metallic ferromagnets, *Nat. Mater.* **15**, 501 (2016).
 - [21] R. Tomasello, M. Ricci, P. Burrascino, V. Puliafito, M. Carpentieri, and G. Finocchio, Electrical detection of single magnetic skyrmion at room temperature, *AIP Adv.* **7**, 056022 (2017).
 - [22] A. Fert, V. Cros, and J. Sampaio, Skyrmions on the track, *Nat. Nanotechnol.* **8**, 152 (2013).

- [23] R. Tomasello, E. Martinez, R. Zivieri, L. Torres, M. Carpentieri, and G. Finocchio, A strategy for the design of skyrmion racetrack memories, *Sci. Rep.* **4**, 6784 (2014).
- [24] X. Zhang, M. Ezawa, and Y. Zhou, Magnetic skyrmion logic gates: Conversion, duplication and merging of skyrmions, *Sci. Rep.* **5**, 9400 (2015).
- [25] J. Müller, A. Rosch, and M. Garst, Edge instabilities and skyrmion creation in magnetic layers, *New J. Phys.* **18**, 065006 (2016).
- [26] D. Pinna, F. A. Araujo, J.-V. Kim, V. Cros, D. Querlioz, P. Bessiere, J. Droulez, and J. Grollier, Skyrmion gas Manipulation for Probabilistic Computing, *Phys. Rev. Appl.* **9**, 064018 (2018).
- [27] J. Zázvorka, F. Jakobs, D. Heinze, N. Keil, S. Kromin, S. Jaiswal, K. Litzius, G. Jakob, P. Virnau, and D. Pinna *et al.*, Thermal skyrmion diffusion used in a reshuffler device, *Nat. Nanotechnol.* **14**, 658 (2019).
- [28] C. Y. You and N. H. Kim, Critical dzyaloshinskii-moriya interaction energy density for the skyrmion states formation in ultrathin ferromagnetic layer, *Curr. Appl. Phys.* **15**, 298 (2015).
- [29] W. Legrand, D. Maccariello, N. Reyren, K. Garcia, C. Moutafis, C. Moreau-Luchaire, S. Collin, K. Bouzehouane, V. Cros, and A. Fert, Room-temperature current-induced generation and motion of sub-100 nm skyrmions, *Nano Lett.* **17**, 2703 (2017).
- [30] J. V. Kim and M. W. Yoo, Current-driven skyrmion dynamics in disordered films, *Appl. Phys. Lett.* **110**, 132404 (2017).
- [31] T. McGuire and R. Potter, Anisotropic magnetoresistance in ferromagnetic 3D alloys, *IEEE Trans. Magn.* **11**, 1018 (1975).
- [32] C. Hanneken, F. Otte, A. Kubetzka, B. Dupé, N. Romming, K. Von Bergmann, R. Wiesendanger, and S. Heinze, Electrical detection of magnetic skyrmions by tunnelling non-collinear magnetoresistance, *Nat. Nanotechnol.* **10**, 1039 (2015).
- [33] A. Kubetzka, C. Hanneken, R. Wiesendanger, and K. Von Bergmann, Impact of the skyrmion spin texture on magnetoresistance, *Phys. Rev. B* **95**, 104433 (2017).
- [34] L. Appeltant, M. C. Soriano, G. Van der Sande, J. Danckaert, S. Massar, J. Dambre, B. Schrauwen, C. R. Mirasso, and I. Fischer, Information processing using a single dynamical node as complex system, *Nat. Commun.* **2**, 468 (2011).
- [35] Y. Paquot, F. Duport, A. Smerieri, J. Dambre, B. Schrauwen, M. Haelterman, and S. Massar, Optoelectronic reservoir computing, *Sci. Rep.* **2**, 287 (2012).
- [36] R. Martinenghi, S. Rybalko, M. Jacquot, Y. K. Chembo, and L. Larger, Photonic Nonlinear Transient Computing with Multiple-Delay Wavelength Dynamics, *Phys. Rev. Lett.* **108**, 244101 (2012).
- [37] D. Brunner, M. C. Soriano, C. R. Mirasso, and I. Fischer, Parallel photonic information processing at gigabyte per second data rates using transient states, *Nat. Commun.* **4**, 1 (2013).
- [38] J. Torrejon, M. Riou, F. A. Araujo, S. Tsunegi, G. Khalsa, D. Querlioz, P. Bortolotti, V. Cros, K. Yakushiji, A. Fukushima, H. Kubota, S. Yuasa, M. D. Stiles, and J. Grollier, Neuromorphic computing with nanoscale spintronic oscillators, *Nature* **547**, 428 (2017).
- [39] G. Finocchio, M. Di Ventra, K. Y. Camsari, K. Everschor-Sitte, P. K. Amiri, and Z. Zeng, The promise of spintronics for unconventional computing, arXiv preprint arXiv:1910.07176 (2019).
- [40] J. Grollier, D. Querlioz, K. Camsari, K. Everschor-Sitte, S. Fukami, and M. D. Stiles, Neuromorphic spintronics, *Nat. Electron.* **3**, 360 (2020).
- [41] L. Berger, Emission of spin waves by a magnetic multilayer traversed by a current, *Phys. Rev. B* **54**, 9353 (1996).
- [42] J. C. Slonczewski, Current-driven excitation of magnetic multilayers, *J. Magn. Magn. Mater.* **159**, L1 (1996).
- [43] I. Dzyaloshinsky, A thermodynamic theory of “weak” ferromagnetism of antiferromagnetics, *J. Phys. Chem. Solids* **4**, 241 (1958).
- [44] T. Moriya, New Mechanism of Anisotropic Superexchange Interaction, *Phys. Rev. Lett.* **4**, 228 (1960).
- [45] A. Thiaville, S. Rohart, É. Jué, V. Cros, and A. Fert, Dynamics of dzyaloshinskii domain walls in ultrathin magnetic films, *EPL (Europhysics Letters)* **100**, 57002 (2012).
- [46] B. Krüger, Current-Driven Magnetization Dynamics: Analytical Modeling and Numerical Simulation (PhD Thesis), (2011).
- [47] A. Vansteenkiste, J. Leliaert, M. Dvornik, M. Helsen, F. Garcia-Sanchez, and B. Van Waeyenberge, The design and verification of mumax3, *AIP Adv.* **4**, 107133 (2014).
- [48] G. Selke, Design and development of a gpu-accelerated micromagnetic simulator, (2014).
- [49] M. Baćani, M. A. Marioni, J. Schwenk, and H. J. Hug, How to measure the local dzyaloshinskii-moriya interaction in skyrmion thin-film multilayers, *Sci. Rep.* **9**, 1 (2019).